Chapter 2

Time-Distance Measurement and Inversion Methods

2.1 Time-Distance Measurement Procedure

Time-distance helioseismology was first introduced by Duvall et al. (1993, 1996), and then greatly improved and widely used in the later studies (see section §1.3.3 for introductions on the major results obtained in the past years. In this chapter, I present the detailed procedure of doing time-distance measurement and inversion problems. The following description is more like a technical note, without including many derivations and theories that can be found in Giles (1999). One should be able to reproduce time-distance measurement by following the descriptions in this chapter, together with some parts of codes and parameters presented in Appendix A.

2.1.1 MDI Data

The Michelson Doppler Imager (MDI) is an instrument dedicated to helioseismology studies aboard the spacecraft *Solar and Heliospheric Observatory (SOHO)*, which was launched in December, 1995. *SOHO* was placed in orbit of Lagrange point L_1 between the Earth and Sun, thus, MDI provided helioseismologists an unprecedented data quality, free of day and night shifts and free of seeing. Since 1996, MDI has provided continuous (with occasional interruption) coverage of medium-l Dopplergrams, full-disk campaign data for a couple of months each year and many high-resolution Dopplergrams, along with magnetic field observations, which are essentially useful to monitor solar activity and are broadly used by the solar community around the world.

The high-resolution MDI Dopplergrams have a spatial resolution of $1''.25$, or $0''.625$ per pixel, which is corresponding to 0.034 heliographic degree per pixel at the center of the solar disk. High resolution data only cover a fraction of solar disk. The full-disk Dopplergrams cover the whole solar disk with 1024×1024 pixels, with a spatial resolution of $2''.0$/pixel, or 0.12 heliographic degrees per pixel. In every year following the launch of *SOHO*, MDI had a campaign period lasting a couple of months or longer, transmitting down continuous full-disk Dopplergrams that are extremely valuable for helioseismic studies. But, due to the limitation of telemetry, this cannot be done all year long. Therefore, MDI has a Structure observation mode, in which the full-disk data are reduced to 192×192 pixels by the onboard computer and then transmitted down every minute. Details on data parameters, data acquisition and transmission are described by Scherrer et al. (1995).

The observation cadence for all the different observational modes is one minute. The one minute cadence gives a Nyquist frequency of 8.33 mHz when doing Fourier transforms, which is fairly good for helioseismology research.

2.1.2 Remapping and Tracking

The Sun is a sphere, and all points on the Sun's surface can be located by their spherical coordinates. It is more convenient to transform the solar region of interests to a Cartesian coordinate system for local helioseismology studies. There are various remapping algorithms for different purposes, and the one used throughout this dissertation is Postel's projection, which is designed to preserve the great circle distance of any points inside the region to the center of the remapped region. It has been shown that if the remapped region is not very large, Postel's projection is good at minimizing the deformation of the power-spectrum and is optimal for local helioseismological studies (Bogart et al., 1995).

Usually, a few to tens of hours of continuous Dopplergrams with one-minute cadence are used for helioseismic studies. In order to keep tracking oscillations of specific locations, the differential rotation rate of the Sun should be removed from the observations. One of the two commonly used tracking rates is the latitude dependent Snodgrass rate (Snodgrass, 1984):

$$\Omega/2\pi\,(\mathrm{nHz}) = 451 - 55\sin^2\lambda - 80\sin^4\lambda \tag{2.1}$$

where λ is latitude; the other tracking rate is a solid Carrington rotation rate: 456 nHz, which is corresponding to the rotation rate of magnetic features at the latitude of 17°. However, if using the tracking command `fastrack`, it should be noted that for a specific tracked region, even if one chooses Snodgrass rate to be removed, the actual rotation rate removed is uniformly the Snodgrass rate at the center of the tracked region rather than a latitude dependent rate. This factor should be taken into consideration when tracking before time-distance analysis, and a tracking over very long time should be avoided to prevent the distortion of high latitude regions after tracking. A datacube is thus ready for use with the first dimension as longitude, second dimension as latitude and the third one as time sequence.

The magnitude of Doppler velocities introduced by solar rotation and by supergranular flows is often much larger than the stochastic oscillations on the solar surface. So, usually, the background image which is obtained by averaging all images of the studied time period is subtracted from every Dopplergram.

2.1.3 Filtering

As in all problems of signal processing, filtering is an essential part of the time-distance measurement.

Surface gravity waves, also known as the fundamental mode (f-mode, the lowest ridge in the k-ω diagram shown in Figure 2.1a), have different origins and different

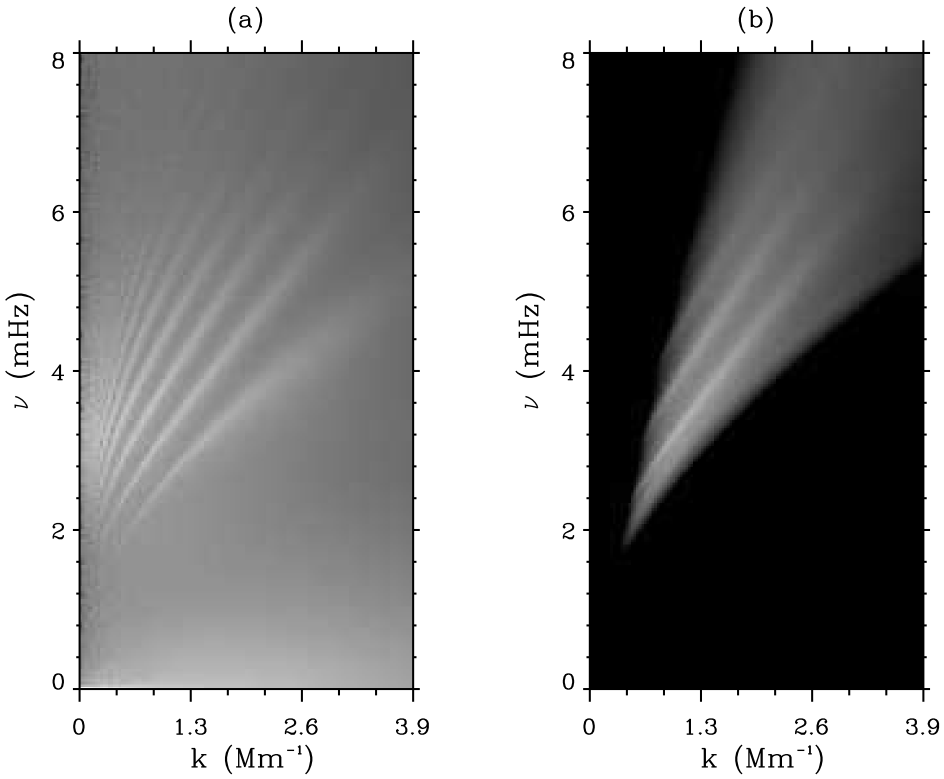

Figure 2.1: (a) The power-spectrum diagram obtained from 512-minute MDI high resolution Dopplergrams; (b) An example of the power-spectrum diagram after f-mode and phase-velocity filtering. This example is corresponding to a case of annulus range: $1\overset{\circ}{.}190 - 1\overset{\circ}{.}598$, with the phase-velocity filter centered at a speed of ~ 25 km/s. Both diagrams are displayed after taking a logarithm of the acoustic power.

properties with the pressure modes (p-modes) that are studied throughout this dissertation. Therefore, the f-mode should be filtered out from the k-ω diagram firstly. The locations of the f-mode and p_1 ridges in the k-ω diagram can be approximated with polynomial forms of (Giles, 1999):

$$\begin{aligned} l_0 &\approx R_\odot k_0 = 100\nu^2 \\ l_1 &\approx R_\odot k_1 = \sum_{k=0}^{4} c_k \nu^k \qquad c = \{17.4, -841, 95.6, -0.711, -0.41\} \end{aligned} \tag{2.2}$$

where the cyclic frequency $\nu \equiv \omega/2\pi$ is measured in milliHertz. A filter is then constructed by use of Gaussian roll-off with full transmission halfway between the f- and p_1- ridges, and no transmission at and below the f-ridge. The f-mode signals are thus filtered out by applying this filter to the k-ω power spectrum.

The phase-velocity filter has turned out to be a very useful tool to strongly improve the signal-noise ratio when the annulus radius is rather small, and this makes mapping the travel times with certain spatial resolution possible. All the waves with the same ratio of ω/k_h travel with the same speed and travel the same distance between bounces off the solar surface, where k_h is the horizontal wavenumber. Therefore, in the Fourier domain, we can design a phase-velocity filter that has a desired phase speed ω/k_h, which is equal to the travel distance divided by the corresponding travel time that can be computed from the ray-approximation based on the solar model, and filter out all other waves which do not have the same phase speed. Such a filter is designed to have a Gaussian shape, with full pass on the line with desired slope, and the full width at half maximum chosen like given in Appendix A. An example of a two-dimensional k-ω diagram obtained from 512-min high resolution MDI data after f-mode filtering and phase-velocity filtering is shown in Figure 2.1. All the necessary parameters for phase-velocity filtering for different annulus ranges used in my study are presented in Appendix A. In practice, the k-ω power spectrum has three dimensions, and one can easily imagine the shape of the three-dimensional phase-velocity filter.

2.1.4 Computing Acoustic Travel Time

The computation of temporal cross-correlation functions between the signals located at two different points on the solar surface is the essential part of time-distance measurement to infer the travel time of acoustic waves from one point to the other through the curved ray paths beneath the solar surface. After the filtering is carried out in the Fourier domain, the datasets are transformed back to the space-time domain by the inverse Fourier transform. Suppose f is a set of time-sequence signals on the solar surface, T is the observation duration, then the temporal cross-correlation

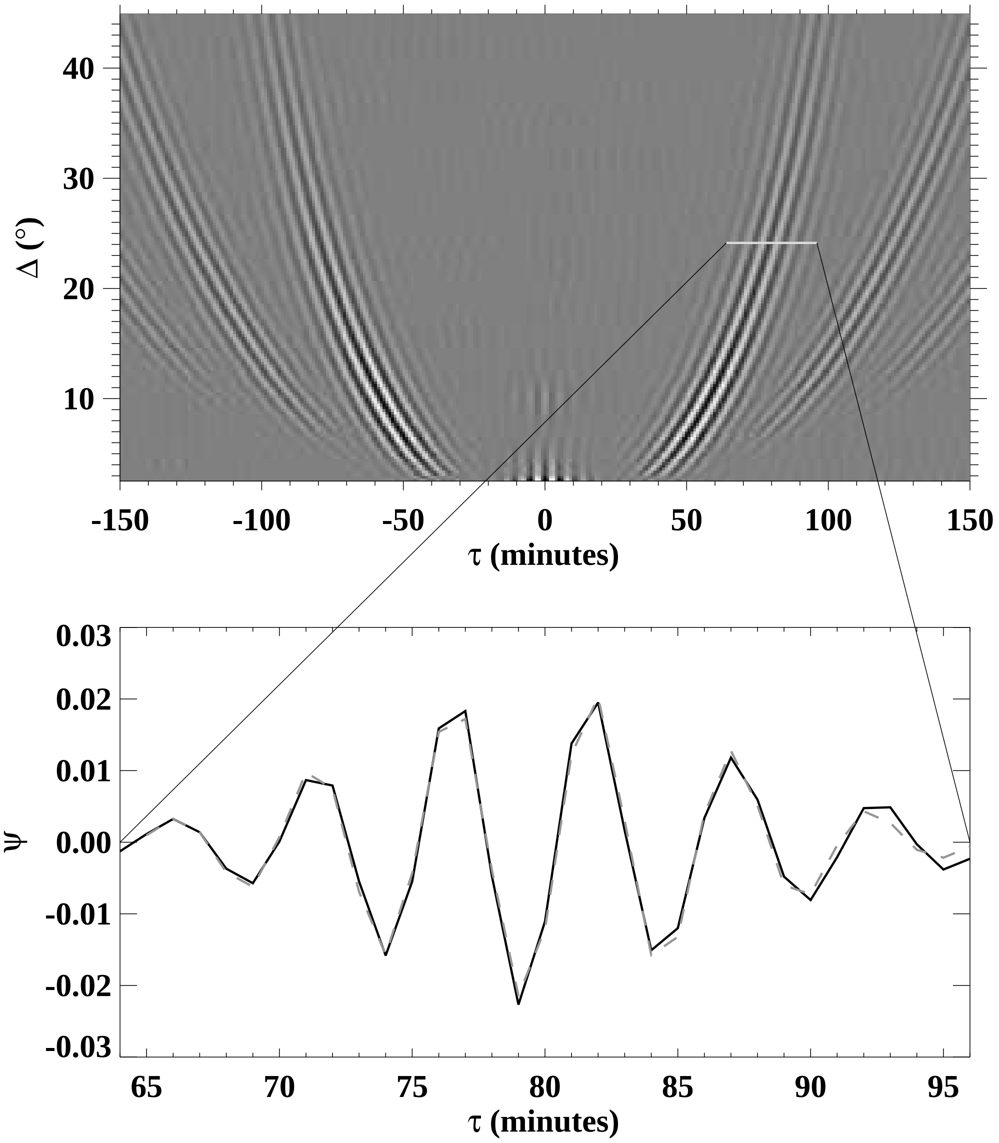

Figure 2.2: Cross-correlation functions for the time-distance measurements. In the upper plot, the gray scale denotes the cross-correlation amplitude as a function of time lag τ and distance Δ. The lower plot shows one cross-correlation function (*solid line*) for $\Delta = 24.^{\circ}1$, and its fitting function (*dashed line*). This plot is adopted from Giles (1999).

function between two different locations $\mathbf{r_1}$ and $\mathbf{r_2}$

$$\Psi(\mathbf{r}_1, \mathbf{r}_2, \tau) = \frac{1}{T}\int_0^T \mathrm{d}t\, f(\mathbf{r}_1, t)\, f(\mathbf{r}_2, t+\tau) \tag{2.3}$$

can be computed. But in practice, the cross-correlation function between two points is often too noisy to be useful; it is practical to compute the cross-correlation function between the signals of a central point and the average signals of all points inside an annulus with a specific distance range to the central point.

Figure 2.2 shows a time-distance diagram and an example of the cross-correlation function for a specific distance. For the case of center-annulus cross-correlation, the part with positive time lag τ is interpreted as the travel time of outgoing waves from the center to its surrounding annulus, and the part with negative lag is interpreted as the travel time of ingoing waves from the surrounding annulus to the central point.

Kosovichev & Duvall (1996) have shown that the cross-correlation function for the time-distance measurement is approximately a Gabor function having a form of:

$$\Psi(\Delta, \tau) = A\cos[\omega_0(\tau - \tau_p)]\exp\left[-\frac{\delta\omega^2}{4}(\tau - \tau_g)^2\right] \tag{2.4}$$

where Δ is the distance between the two points, i.e., $\Delta = |\mathbf{r_1} - \mathbf{r_2}|$, A is the cross-correlation amplitude, ω_0 is the central frequency of the wave packet, τ_p and τ_g are the phase and group travel times, and $\delta\omega$ is the frequency bandwidth. Among these parameters, $A, \omega_0, \tau_p, \tau_g$ and $\delta\omega$ are free parameters to be determined by fitting the cross-correlation function computed from real data by applying a non-linear least squares fitting method. The subroutine used for the non-linear least squares fitting is based on the code `mrqmin` in §15.5 of *Numerical Recipes in FORTRAN 77: the Art of Scientific Computing* (Second Edition); or alternatively, the procedure `lmfit.pro` provided by IDL can be used directly. An IDL code to perform the fitting by use of `lmfit.pro` is given in Appendix A. In practice, it turns out that the phase travel time τ_p is often more accurately determined than the group travel time τ_g in the fitting procedure, and will be used to represent wave travel time throughout this dissertation unless specified otherwise.

2.1.5 Constructing Maps of Travel Times

For one specific location, after outgoing and ingoing travel times are computed, one can derive the mean travel time variations and travel time differences for this location:

$$\delta\tau^{\rm oi}_{\rm mean}(\mathbf{r},\Delta) = \frac{\tau^+ + \tau^-}{2} - \langle\tau\rangle, \qquad \delta\tau^{\rm oi}_{\rm diff}(\mathbf{r},\Delta) = \tau^+ - \tau^- \tag{2.5}$$

where τ^+ and τ^- indicate the outgoing and ingoing travel times, respectively, and $\langle\tau\rangle$ represents the theoretical travel time for this specific annulus range. $\delta\tau^{\rm oi}_{\rm mean}$ and $\delta\tau^{\rm oi}_{\rm diff}$ are the measurements which are going to be used directly to do inversions to infer the sound-speed variations and flow fields of the solar interior. If we move the central point to another location, and repeat the above procedure, the $\delta\tau^{\rm oi}_{\rm mean}$ and $\delta\tau^{\rm oi}_{\rm diff}$ can be measured for this point. Thus, we can select every pixel inside the region of interest to calculate the corresponding travel times, and obtain a map of the travel times, as shown in Figure 2.3(a) and (b).

Above, the center-annulus cross-correlation is computed to derive mean travel times and travel time differences. In order to have more measurements as inputs to do inversions, we divide the circular annulus into four quadrants, corresponding to East, West, North and South directions. The cross-correlation functions between average signals inside these quadrants and the signal of the central point are computed, respectively, and then the East-center and center-West functions are combined to derive the West-East travel time differences $\delta\tau^{\rm we}_{\rm diff}$. Similarly, the North-South travel time differences $\delta\tau^{\rm ns}_{\rm diff}$ are derived. It is often thought that $\delta\tau^{\rm we}_{\rm diff}$ is more sensitive to the West-East velocity and $\delta\tau^{\rm ns}_{\rm diff}$ more sensitive to the North-South velocity. The maps for $\delta\tau^{\rm we}_{\rm diff}$ and $\delta\tau^{\rm ns}_{\rm diff}$ can also be made in the same way as $\delta\tau^{\rm oi}_{\rm diff}$, examples are shown in Figure 2.3(c) and (d). Usually, the maps for mean travel times $\delta\tau^{\rm oi}_{\rm mean}$ are used to do inversions for interior sound-speed variation; the maps for $\delta\tau^{\rm oi}_{\rm diff}$, $\delta\tau^{\rm we}_{\rm diff}$ and $\delta\tau^{\rm ns}_{\rm diff}$ are combined as inputs to do inversions for subsurface flow fields.

We then change the annulus radius to repeat all the above procedures to make another set of measurements. Since the ray path of small annuli reaches shallow solar interiors and the ray path of long annuli reach the deep interiors, the appropriate

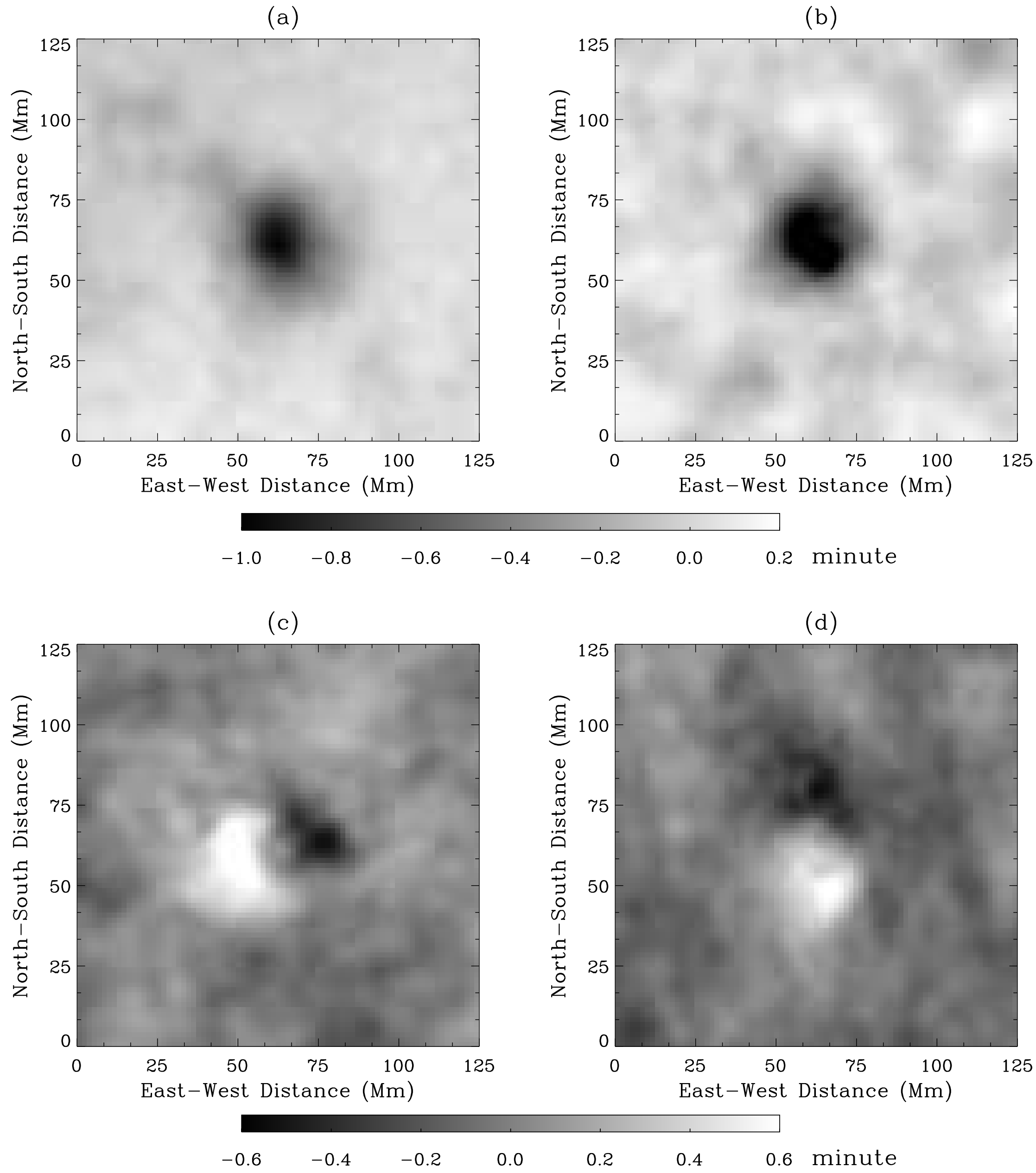

Figure 2.3: The maps of travel times for a solar region including a sunspot: (a) Mean travel times $\delta\tau^{\rm oi}_{\rm mean}$; (b) Outgoing and ingoing travel time differences $\delta\tau^{\rm oi}_{\rm diff}$; (c) East- and West-going travel time differences $\delta\tau^{\rm we}_{\rm diff}$; (d) North- and South-going travel time differences $\delta\tau^{\rm ns}_{\rm diff}$. The annulus ranges used to obtain these maps are $1^\circ\!.19 - 1^\circ\!.598$.

combinations of annulus choices can cover the depths from the solar surface to approximately 20 – 30 Mm in depth. Inversions are then applied on such measurements to derive the sound-speed structure and flow fields at different depths.

2.2 Ray-Approximation Inversion Kernels

In order to do time-distance inversions, we need to have inversion kernels that could be derived from a solar model. In this section, I describe how to derive the inversion kernels based on the ray-approximation, and the compare ray-approximation kernels and wave-approximation kernels.

2.2.1 Ray Paths

The acoustic waves traveling downward from the solar surface are continuously refracted due to the increasing acoustic propagation speed with the depth. Eventually, the waves will turn around and return toward the surface, where they get reflected back from the layer with acoustic cutoff frequency $\omega_{\rm ac}$. The acoustic modes with wavelengths small compared to the solar radius $R_\odot$ are amenable to ray treatment (Gough, 1984). Throughout this dissertation, the ray-approximation is employed to make inversion kernels though the derivation of wave-approximation kernels is currently under development (Birch et al., 2001; Gizon & Birch, 2002). The following content and equations on the ray-approximation largely follow the contents in D'Silva & Duvall (1995).

In polar coordinates, the ray equation for the acoustic mode (ν, l) is

$$\frac{\mathrm{d}r}{r\mathrm{d}\theta} = \frac{v_{\rm gr}}{v_{\rm gh}}\,, \tag{2.6}$$

where $v_{\rm gr}$ and $v_{\rm gh}$ are the radial and horizontal components of the group velocity, and they are expressed as

$$\begin{aligned} v_{\text{gr}} &= \frac{\partial \omega}{\partial k_r} = \frac{k_r \omega^3 c^2}{\omega^4 - k_h^2 c^2 \omega_{\text{BV}}^2}, \\ v_{\text{gh}} &= \frac{\partial \omega}{\partial k_h} = k_h \omega c^2 \Big(\frac{\omega^2 - \omega_{\text{BV}}^2}{\omega^4 - k_h^2 c^2 \omega_{\text{BV}}^2} \Big), \end{aligned} \tag{2.7}$$

where the radial and horizontal wavenumbers k_r and k_h are given by the local dispersion relations

$$\begin{aligned} k_r^2 &= \frac{1}{c^2}(\omega^2 - \omega_{\text{ac}}^2) - k_h^2 \Big(1 - \frac{\omega_{\text{BV}}^2}{\omega^2} \Big), \\ k_h^2 &= \frac{L^2}{r^2} = \frac{l(l+1)}{r^2}. \end{aligned} \tag{2.8}$$

In the above equations, ω_{BV} is the Brunt-Väisälä frequency, given by

$$\omega_{\text{BV}}^2 = g \Big(\frac{1}{\Gamma_1} \frac{\mathrm{d} \ln p}{\mathrm{d} r} - \frac{\mathrm{d} \ln \rho}{\mathrm{d} r} \Big), \tag{2.9}$$

where $\Gamma_1 = (\partial \ln p / \partial \ln \rho)_s$ is the adiabatic index and g is the gravity at radius r. The acoustic cutoff frequency ω_{ac} is given by

$$\omega_{\text{ac}}^2 = \frac{c^2}{4 H_\rho^2} \Big(1 - 2 \frac{\mathrm{d} H_\rho}{\mathrm{d} r} \Big), \tag{2.10}$$

where H_ρ is the density scale height

$$H_\rho = - \Big(\frac{\mathrm{d} \ln \rho}{\mathrm{d} r} \Big)^{-1}. \tag{2.11}$$

Once we have all the above equations for the ray approximation, by use of the solar model S (Christensen-Dalsgaard et al., 1996) in practice, we can compute the ray paths for certain acoustic waves with certain acoustic frequency ω and spherical harmonic degree l. The one-skip distance is obtained by integrating the ray equation (2.6) for an initial position (r_1, θ_1). The integration is carried on till the mode turns around at the turning point (r_2, θ_2), where the Lamb frequency $\sqrt{l(l+1)}c/r$ approaches ω and k_r goes to zero. The one-skip distance, or the travel distance of

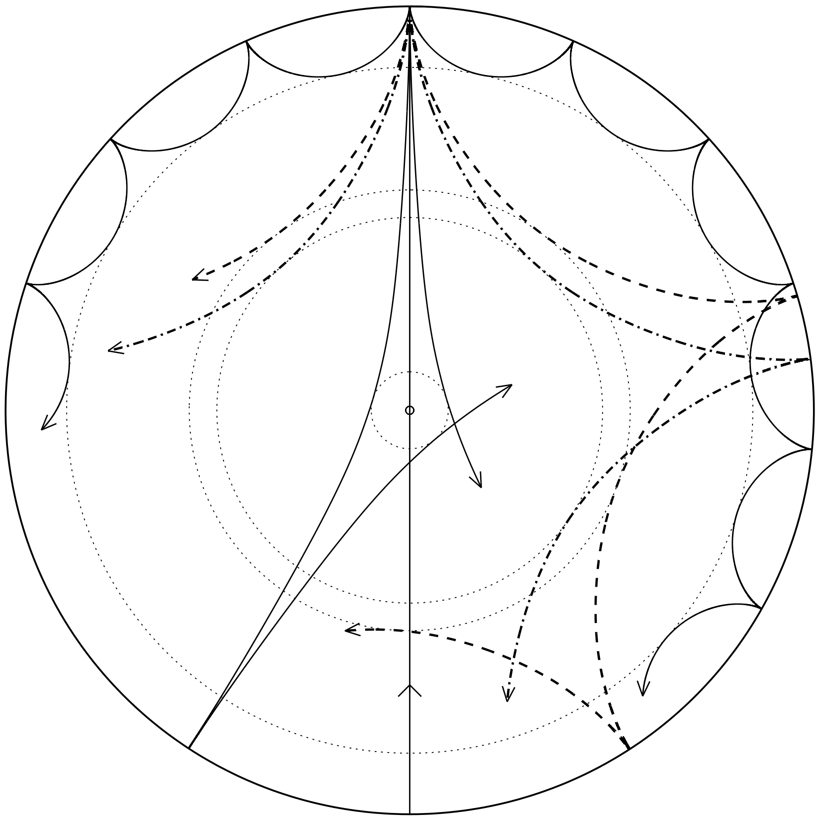

Figure 2.4: A diagram of several ray-paths, showing the different modes of rays reach different depths of solar interior. This plot is adopted from Christensen-Dalsgaard (2002).

the ray, is defined as the angular distance between photospheric reflection points:

$$\Delta = 2|(\theta_2 - \theta_1)|. \tag{2.12}$$

After the ray-path is determined, and the phase velocity at specific locations is known, the corresponding phase travel time can be computed from

$$\tau_p = \int_\Gamma \frac{k\mathrm{d}s}{\omega} = \int_\Gamma \frac{\mathrm{d}s}{v_p} \tag{2.13}$$

where Γ is the ray path. Although this is a simple equation, it is the basis for solving time-distance inversion problems.

2.2.2 Travel Time Perturbation

The following content largely follows the descriptions in Kosovichev et al. (1997). In the ray-approximation, the travel times are only sensitive to the perturbations along the ray paths. The variations of travel times obey Fermat's Principle (e.g., Gough, 1993)

$$\delta\tau = \frac{1}{\omega}\int_{\Gamma} \delta\mathbf{k}\,\mathrm{d}s \tag{2.14}$$

where $\delta\mathbf{k}$ is the perturbation of the wave vector due to the structural inhomogeneities and flows along the unperturbed ray path Γ.

In the solar convection zone, the Brunt-Väisälä frequency $\omega_{\rm BV}$ is small compared to the acoustic cutoff frequency and the typical solar oscillation frequencies, and will be neglected in the following derivations. Thus, after considering the effects caused by the presence of magnetic field, the dispersion relation can be simplified as

$$(\omega - \mathbf{k}\cdot\mathbf{v})^2 = \omega_{\rm ac}^2 + \mathbf{k}^2 c_f^2, \tag{2.15}$$

where $\mathbf{v}$ is the three-dimensional velocity and c_f is the fast magnetoacoustic speed

$$c_f^2 = \frac{1}{2}\left(c^2 + c_A^2 + \sqrt{(c^2+c_A^2)^2 - 4c^2(\mathbf{k}\cdot\mathbf{c}_A)^2/k^2}\right) \tag{2.16}$$

where $\mathbf{c}_A = \mathbf{B}/\sqrt{4\pi\rho}$ is the Alfvén velocity, $\mathbf{B}$ is the magnetic field strength and ρ is the plasma density. To first-order in $\mathbf{v}$, δc, $\delta\omega_{\rm ac}$, and $\mathbf{c}_A$, equation (2.14) becomes

$$\delta\tau^{\pm} = -\int_{\Gamma}\left[\frac{\pm\mathbf{n}\cdot\mathbf{v}}{c^2} + \frac{\delta c}{c}\frac{k}{\omega} + \frac{\delta\omega_{\rm ac}}{\omega_{\rm ac}}\frac{\omega_{\rm ac}^2}{c^2\omega^2}\frac{\omega}{k} + \frac{1}{2}\left(\frac{c_A^2}{c^2} - \frac{(\mathbf{k}\cdot\mathbf{c}_A)^2}{k^2c^2}\right) + \epsilon\right]\mathrm{d}s \tag{2.17}$$

where $\mathbf{n}$ is a unit vector tangent to the ray, and $\delta\tau^{\pm}$ denotes the perturbed travel times along the ray path ($+\mathbf{n}$) and opposite to the ray path ($-\mathbf{n}$). In equation (2.17), ϵ represents some other contributions that are difficult to quantify, such as phase differences caused by wave reflection and observing errors in Dopplergrams. The effects of flows and structural perturbations can be separated by taking the difference

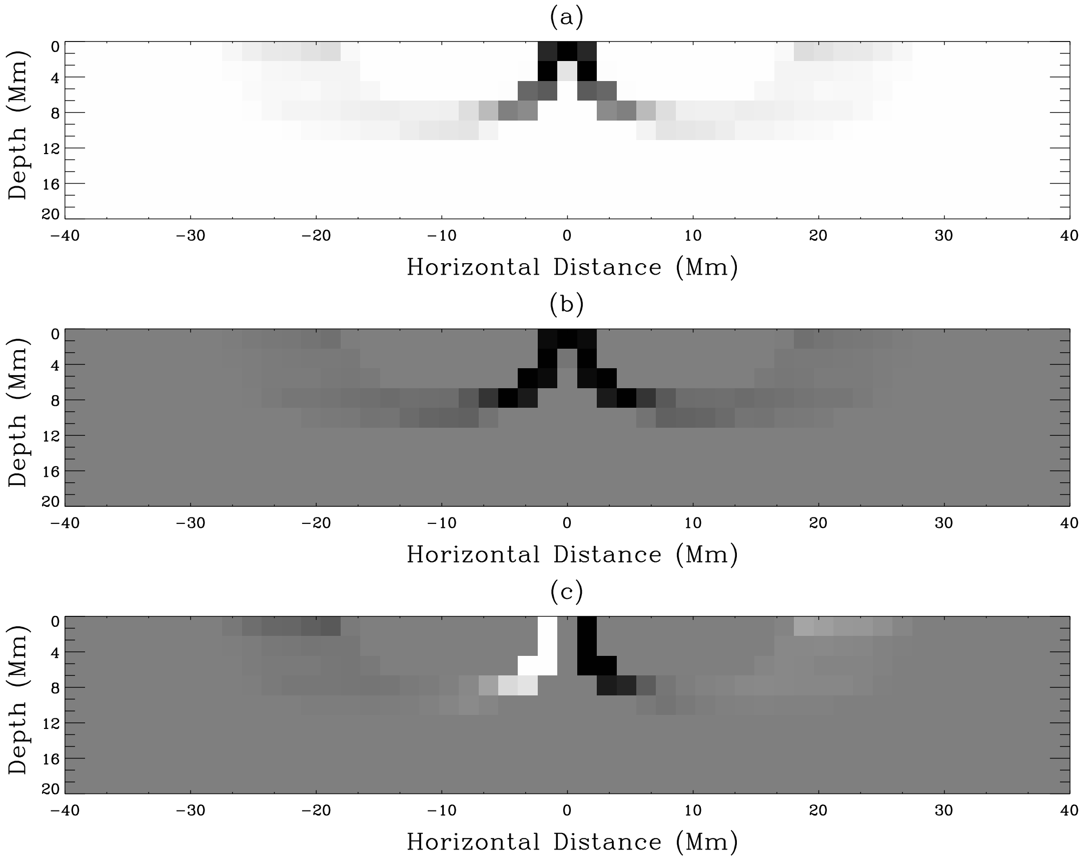

Figure 2.5: Vertical cuts of ray-approximation inversion kernels. (a) Sound-speed kernel for measurement $\delta\tau^{\mathrm{oi}}_{\mathrm{mean}}$; (b) Vertical velocity kernel for measurement $\delta\tau^{\mathrm{oi}}_{\mathrm{diff}}$; (c) Horizontal velocity kernel for measurement $\delta\tau^{\mathrm{oi}}_{\mathrm{diff}}$. These kernels are corresponding to the annulus ranges 1°.598 to 2°.414.

and the mean of the reciprocal travel times:

$$\delta\tau_{\mathrm{diff}} = -2\int_{\Gamma}\frac{\mathbf{n}\cdot\mathbf{v}}{c^2}\mathrm{d}s, \tag{2.18}$$

$$\delta\tau_{\mathrm{mean}} = -\int_{\Gamma}\left[\frac{\delta c}{c}\frac{k}{\omega} + \frac{\delta\omega_{\mathrm{ac}}}{\omega_{\mathrm{ac}}}\frac{\omega_{\mathrm{ac}}^2}{c^2\omega^2}\frac{\omega}{k} + \frac{1}{2}\left(\frac{c_A^2}{c^2} - \frac{(\mathbf{k}\cdot\mathbf{c}_A)^2}{k^2c^2}\right) + \epsilon\right]\mathrm{d}s. \tag{2.19}$$

Equation (2.18), though simple, provides the link between the measured travel time differences and the solar interior velocity, and thus gives us a useful tool to determine the solar subsurface flow fields. Ideally, equation (2.19) can be used to derive the sound-speed perturbation structures, and the anisotropy of the term with $\mathbf{c}_A$ may be used to derive the Alfvén velocity, hence the magnetic field strength. Despite the efforts by Ryutova & Scherrer (1998), no significant progress has been made to disentangle the effects caused by the presence of the magnetic field from the sound-speed perturbation. One useful idea, which I tried, is to make more measurements of travel times in different directions, that is, in addition to the measurements of $\tau_{\rm oi}, \tau_{\rm we}$ and $\tau_{\rm ns}$, we can make the travel time measurements of quadrants northeast-southwest and northwest-southeast. Therefore, more information on anisotropy is obtained, and those measurements help change the inversion problem from being under-determined to be well determined. However, we now have effects from sound-speed variation, flow fields and Alfvén speed perturbation, the combination of which makes the inversion problem very complicated and difficult to solve. Clearly, more efforts could be made in order to make such an inversion possible, and make the derivation of subsurface magnetic field strength possible, which should be very interesting.

2.2.3 Ray-Approximation and Wave-Approximation Kernels

Based on the equations presented in the above two sub-sections and by use of the solar model S (Christensen-Dalsgaard et al., 1996), we compute the ray-approximation inversion kernels for both sound-speed perturbations and three-dimensional flow velocities.

The computation of the ray-approximation kernels closely resemble the procedure of time-distance measurements. Say, for the case of center-annulus measurement, we compute the ray paths and phase travel times from the central point to all the points inside the surrounding annulus, then the paths and travel times are averaged onto grids with the same spatial resolution as the measurements. Corresponding to the measurements of $\delta\tau^{\rm oi}_{\rm diff}$ and $\delta\tau^{\rm oi}_{\rm mean}$, the sensitivity kernels for the sound-speed perturbation, horizontal velocities (v_x and v_y) and vertical velocity (v_z) are computed respectively, as shown in Figure 2.5. The inversion kernels for the v_x, v_y and v_z are also obtained in the same way for measurements of $\delta\tau^{\rm we}_{\rm diff}$ and $\delta\tau^{\rm ns}_{\rm diff}$, the plots of which

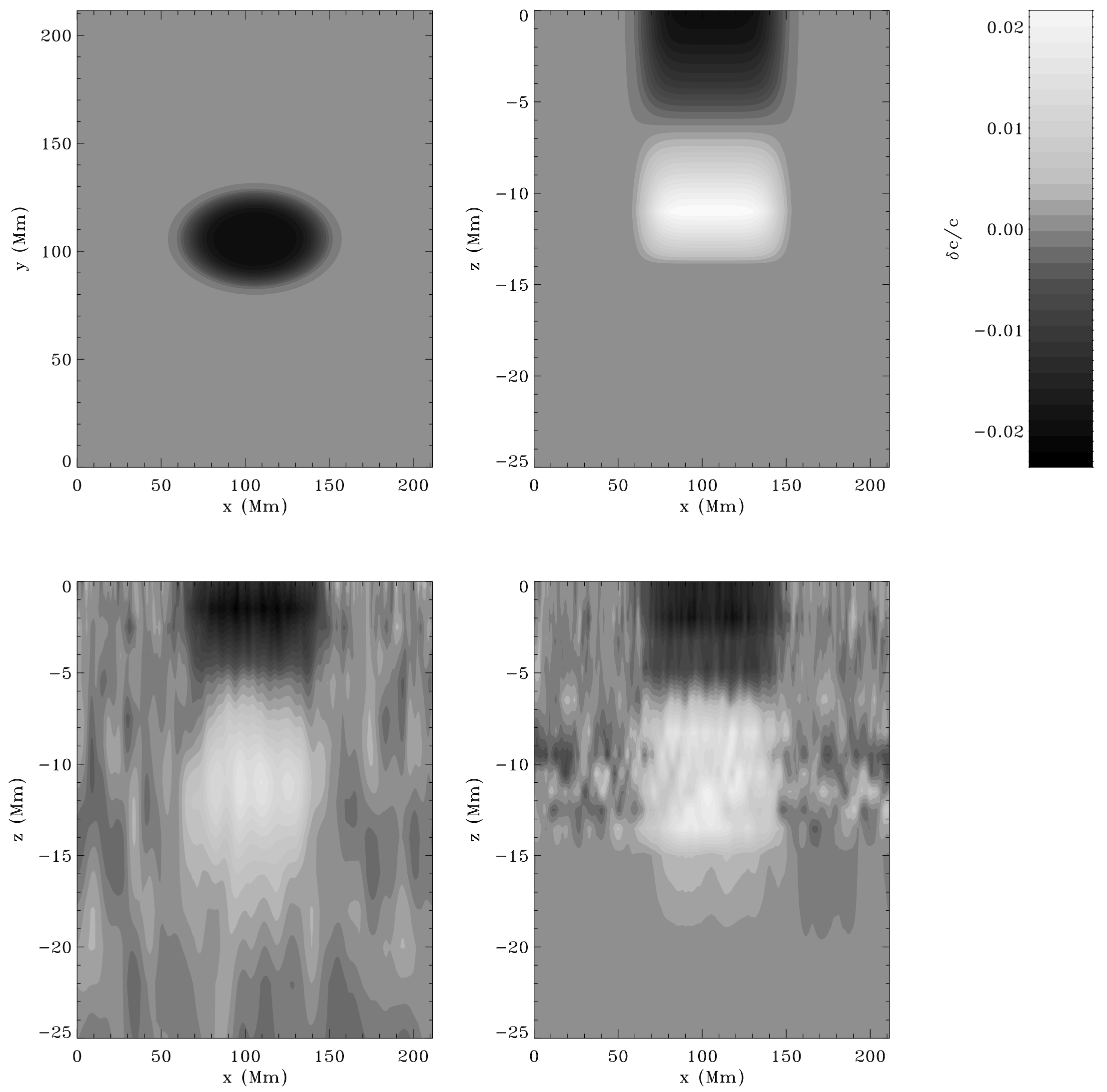

Figure 2.6: An artificial sunspot model and the inversion results. The gray scale represents the sound-speed variations. *Upper*: the surface layer (*left*) and a vertical cut (*right*) of an artificial sunspot model that is to mimic the results presented by (Kosovichev, Duvall, & Scherrer, 2000). The forward problem is performed based on this model to derive the mean travel times, which are then used to do inversions. *Lower*: the inversion result from Fresnel-zone approximation (*left*) and ray-approximation (*right*) kernels. This plot is adopted from Couvidat et al. (2004).

are not shown. Therefore, for each measurement of $\delta\tau_{\text{diff}}^{\text{oi}}$, $\delta\tau_{\text{diff}}^{\text{we}}$, and $\delta\tau_{\text{diff}}^{\text{ns}}$ with each different annulus range, we have a set of inversion kernels corresponding to v_x, v_y and v_z.

It is natural that the ray-approximation may not be the best approximation of the acoustic waves inside the Sun, and the Fresnel-zone approximation (Jensen, Jacobsen, & Christensen-Dalsgaard, 2000) and Born-approximation (Birch & Kosovichev, 2000) are currently under development. Birch et al. (2001) pointed out that for perturbations with radii larger than the first Fresnel-zone, the Born and ray approximations are nearly equivalent; for smaller scale perturbations, the ray approximation may overestimate the travel times significantly. But considering the fact that large amounts of data are involved in measurement and inversion, together with the choice of different regularization types and regularization parameters, it is not immediately clear how the inversion results differ based on different inversion kernels.

Recently, Couvidat et al. (2004) made some intensive comparisons between inversion results based on sensitivity kernels obtained in the ray-approximation and the Fresnel-zone approximation. Different kinds of artificial sound-speed variation structures to simulate sunspot models were made, and the forward problem was performed to derive mean travel times. Then inversions were carried out by utilizing both ray-approximation and Fresnel-zone approximation inversion kernels. The comparison of inversion results shows that, for the sound-speed perturbation, both kernels reveal similar interior structures with similar accuracy in the solar layers shallower than a depth of approximately 15 Mm. Below 15 Mm, however, the ray-approximation can hardly reveal the deeper structures where the Fresnel-zone approximation still works. Figure 2.6 shows one example. It was concluded that the use of Fresnel-zone kernels should not invalidate the results obtained from ray-approximation, provided that the inverted structures lie entirely within the scope of ray-path kernels used. Although the wave approximation inversion kernels for velocities have not been available for comparison, it may be true that similar conclusion can be drawn as for the sound-speed perturbations.

2.3 Inversion Techniques

2.3.1 LSQR Algorithm

Equations (2.18) and (2.19) have shown us the connection between the measured travel times and solar interior properties: sound-speed variations and flow fields. We rewrite these two equations here, dropping the insignificant (presumably) terms in the mean travel times equation:

$$\delta\tau_{\mathrm{diff}} = -2\int_{\Gamma} \frac{\mathbf{v}(\mathbf{r})\cdot\mathbf{n}}{c_0^2(\mathbf{r})}\mathrm{d}s \tag{2.20}$$

$$\delta\tau_{\mathrm{mean}} = -\int_{\Gamma} \frac{\delta c(\mathbf{r})}{c_0^2(\mathbf{r})}\mathrm{d}s \tag{2.21}$$

We can divide the three-dimensional region into rectangular blocks, and study the properties inside the blocks as a discrete model. Assume that the sound-speed perturbation, $\delta c/c$, and the ratio of flow velocity to the sound-speed, $\mathbf{v}/c$, are constant in each block and remain unchanged during the observation period, then we can linearize the above equations to obtain:

$$\delta\tau_{\mathrm{mean}}^{\lambda\mu\nu} = \sum_{ijk} A_{ijk}^{\lambda\mu\nu}\frac{\delta c_{ijk}}{c_{ijk}}, \tag{2.22}$$

$$\delta\tau_{\mathrm{diff}}^{\lambda\mu\nu} = \sum_{ijk,\alpha} B_{ijk,\alpha}^{\lambda\mu\nu}\frac{v_{ijk,\alpha}}{c_{ijk}}, \tag{2.23}$$

where $A_{ijk}^{\lambda\mu\nu}$ and $B_{ijk,\alpha}^{\lambda\mu\nu}$ are the inversion kernels obtained by the ray-approximation based on the descriptions in the last section. Here, λ and μ label the points inside the observed area, and ν labels different annulus ranges, and in most cases of this dissertation is $1 \le \nu \le 11$; i, j and k are the indices of the blocks in three dimensions; and α denotes the three components of the flow velocity.

If transforming matrix $B_{ijk,\alpha}^{\lambda\mu\nu}$ into a square matrix, one side of this matrix is, typically, as large as $128\times128\times11\times11\times3$, so equations (2.22) and (2.23) are typical large sparse linear equations which can be solved in the sense of least squares. LSQR is an algorithm proposed by Paige & Saunders (1982) to solve the linear problems

$Ax = y$ or least squares problems $\min||Ax - y||_2$. This algorithm was later widely used in geophysical inverse problems, and helioseismological inverse problems (e.g., Kosovichev, 1996).

The LSQR algorithm is based on the bidiagonalization procedure of Golub & Kahan (1965), and it is analytically equivalent to the standard method of conjugate gradients. It was demonstrated to be more reliable than other algorithms when the coefficients matrix A is ill-conditioned, which is actually the case of our inverse problems. The great advantage of the LSQR algorithm is that it is an iterative method and avoids the computation of the inverse of a large sparse matrix (which is often unstable and involves a great amount of computation). In practice, it is only required for the users to provide the computation of Ax and $A^T y$ for each step of the iteration. This algorithm also has a build-in zero-th order regularization, or damping coefficient, which is to minimize $||x||_2$ and $||Ax - y||_2$ at the same time. We have not found a way to incorporate the first-order or second-order Tikhonov regularization into this algorithm easily and efficiently, except to do that externally by providing an additional dimension of coefficient matrix A.

Because of the extremely large size of the matrices involved, the computation burden of the inversion is also very heavy. Fortunately, it was found that the direct matrix multiplications of Ax and $A^T y$, the core part of the computation and where the most computation time is spent, can be converted into convolution problems, which expedite the computations by a factor of about 20 times in my computations. Later, BLAS library and FFTW package for fast Fourier transforms were employed in the inversion code, which reduced the computation time from the original a couple of days down to a couple of minutes.

There are a few other issues which should be addressed about LSQR algorithm, such as the ability to detect deeper structures, vortical flows, cross-talk, and the spatial resolution. I plan to incorporate such discussions into following chapters when dealing with the particular inversion problems.

2.3.2 Multi-Channel Deconvolution (MCD)

As pointed out in last section, the very large matrix multiplication Ax can be transformed into a convolution. Therefore, it it possible to solve the least square problem in the Fourier domain, which may expedite the computation speed and also provide us an alternative way to do inversions. A multi-channel deconvolution (MCD) technique was developed and have been used in solving local helioseismic problems (Jacobsen et al., 1999; Jensen, Jacobsen, & Christensen-Dalsgaard, 1998).

In the following, I derive the equations for the case of sound-speed perturbations, the equations for three-dimensional velocities can be derived similarly, but with one more dimension. As shown in the last section, we have obtained the discrete equation (2.22) for the sound-speed perturbation:

$$\delta\tau^{\lambda\mu\nu}_{\mathrm{mean}} = \sum_{ijk} A^{\lambda\mu\nu}_{ijk}\delta s_{ijk} \tag{2.24}$$

where I use δs_{ijk} to replace $\delta c_{ijk}/c_{ijk}$. By considering the measurement procedure of time-distance, this equation is actually equivalent to a convolution, which is then simplified as a direct multiplication in the Fourier domain:

$$\delta\tilde{\tau}^{\nu}(\kappa_\lambda,\kappa_\mu) = \sum_k \tilde{A}^{\nu}_k(\kappa_\lambda,\kappa_\mu)\delta\tilde{s}_k(\kappa_\lambda,\kappa_\mu) \tag{2.25}$$

where $\delta\tilde{\tau}$, $\tilde{A}$ and $\delta\tilde{s}$ are the Fourier transforms of $\delta\tau$, A and δs, respectively; $\kappa_\lambda, \kappa_\mu$ are the wavenumbers in the Fourier domain corresponding to λ, μ in the space domain. For each specific $(\kappa_\lambda, \kappa_\mu)$, the equation in the Fourier domain is a direct matrix multiplication:

$$d = Gm \tag{2.26}$$

where

$$G = \left\{\tilde{A}^{\nu}_k(\kappa_\lambda,\kappa_\mu)\right\}, \quad d = \left\{\delta\tilde{\tau}^{\nu}(\kappa_\lambda,\kappa_\mu)\right\}, \quad m = \left\{\delta\tilde{s}_k(\kappa_\lambda,\kappa_\mu)\right\}$$

Thus, we have a large number of small linear equations in the Fourier domain. If all these small linear equations can be solved to obtain m for all $(\kappa_\lambda, \kappa_\mu)$, then the two-dimensional m can be inverse Fourier transformed back to the space domain to obtain all the values of δs_{ijk} that we are seeking.

Equation (2.26) is a small linear complex equation that can be solved in numerous ways. Here, we adopt the method given by Menke (1984), and solve the equations by:

$$m = \left(G^H G + \varepsilon^2 V\right)^{-1} G^H d \tag{2.27}$$

where G^H is the conjugate transpose of G, ε can be viewed as a damping parameter, and V is a diagonal matrix chosen as

$$V = \begin{pmatrix} 1 & 0 & 0 & \dots & 0 \\ 0 & \frac{c_2}{c_1} & 0 & \dots & 0 \\ 0 & 0 & \frac{c_3}{c_1} & \dots & 0 \\ \vdots & \vdots & \vdots & \ddots & \vdots \\ 0 & 0 & 0 & \dots & \frac{c_N}{c_1} \end{pmatrix}$$

where c_N is the sound-speed at the N-th layer from the solar model used.

Just like the damping coefficient λ used in the LSQR algorithm, the choice of ε in MCD is somewhat arbitrary. Often, many artificial tests are performed to choose a reasonable value of ε in practice. Since each small linear equation is solved in the Fourier domain, the first-order or second-order regularization can only be applied in the vertical direction. But on the other hand, because it is in the Fourier domain, the reasoning and effects of applying first- or second-order regularization is vague.

2.3.3 Comparison of LSQR and MCD

Previously, it was argued that MCD had great advantage in computing time over iterative solvers such as LSQR (Jensen, Jacobsen, & Christensen-Dalsgaard, 1998). However, after I utilized the convolution to compute the matrix multiplication, and incorporated the BLAS library and FFTW package into the LSQR technique, the computing time advantage of MCD was gone. Currently, both codes can finish the computation of a typical inverse problem (say, 128×128 in horizontal and 11 in vertical direction) within a couple of minutes on a Pentium IV machine with a speed of 2.0 GHz and a memory of 1.0 GB. The computation time increases with the same

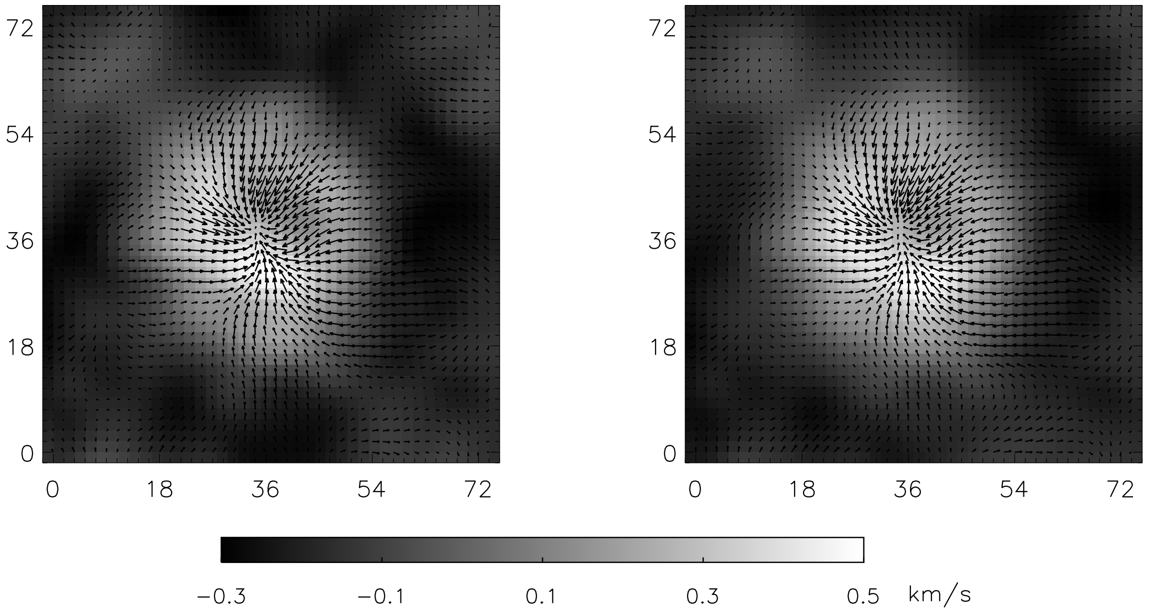

Figure 2.7: Comparison of LSQR algorithm and MCD inversions on the subsurface flow fields of a sunspot. The maps are obtained at the depth of 0 – 3 Mm. In each image, lighter represent downward flows and darker represent upward flows. Arrows in the graph represent horizontal flows, with longest arrow as 1 km/s approximately. Horizontal scales are in units of Mm.

ratio as the increase of the size of the three-dimensions of the inverted region, provided that the memory requirement does not exceed the computer's memory limit.

Then, the next issue is to compare the accuracy of results obtained by these two different inversion techniques. We applied both LSQR and MCD techniques on the same time-distance measurements of a sunspot to derive the subsurface flow fields that will be shown in Chapter 3. Figure 2.7 shows a comparison of the three-dimensional flow fields obtained at the depth of 0 – 3 Mm. Clearly, both horizontal velocities and the vertical velocities agree very well with each other. The correlation coefficients between the three dimensional velocities obtained by these two different techniques are all above 95% at different depths shallower than 12 Mm.

The differences between these two inversion techniques may come from the choice of damping coefficients: λ for LSQR and ε for MCD. LSQR solves the equation iteratively in the space domain, and MCD solves the problem in Fourier domain, whereas the choice of damping coefficient can hardly agree with each other. Our comparison shown above may and may not reflect the best match of these two regularization parameters.